Bulg. J. Phys. **32** (2005) 237–256

# Electronic and Vibrational Properties of Single-Walled Carbon Nanotubes

**V. N. Popov**[1], **Ph. Lambin**[2]

[1]Faculty of Physics, University of Sofia, BG-1164 Sofia, Bulgaria

[2]Facultés Universitaires Notre-Dame de la Paix, B-5000 Namur, Belgium

Received

**Abstract.** The implementation of a symmetry-adapted scheme to the study of the electronic and vibrational properties of single-walled carbon nanotubes is presented. The usually very large number of carbon pairs in the unit cell of the nanotubes, that hinders most of the microscopic studies, is conveniently handled in this approach by using the screw symmetry of the nanotubes and a two-atom unit cell. This scheme allows the systematic simulation of various properties (vibrational, mechanical, thermal, electronic, optical, dielectric, etc.) of all nanotubes of practical interest. The application of symmetry-adapted models to the study of some of these properties is illustrated in two cases: a force-constant approach and a tight-binding approach.

PACS number: 63.22.+m, 73.63.Fg, 78.30.Na

## 1 Introduction

The discovery of the carbon nanotubular structures in 1991 led to an avalanche of theoretical and experimental work motivated by their unusual properties and the possibility for their industrial application [1]. Nowadays, carbon nanotubes are components of composite materials, various field-effect devices, field-emitters in displays, hydrogen storage devices, gas sensors, etc. The theoretical study of the nanotubes is based on the use of an idealized structure: a uniform cylinder or an atomic structure with one-dimensional periodicity. The practical calculations in the latter case face an often insurmountable obstacle arising from the necessity to deal with a large number of carbon atoms. This hindrance can be overcome considering a usually neglected symmetry of the ideal nanotubes, the screw symmetry. In this paper, we show how the explicit use of the screw symmetry allows the easy computational handling of practically all existing nanotube types. This is illustrated on the example of the lattice dynamics and electronic band structure calculations of nanotubes using a force-constant approach and a tight-binding

approach. The theoretical predictions are compared to available theoretical and experimental data.

## 2 The Nanotube Structure

The ideal single-walled carbon nanotube can be viewed as obtained by rolling up an infinite graphite sheet (graphene) into a seamless cylinder leading to coincidence of the lattice point O at the origin and a point A with indices $(L_1, L_2)$ defining the chiral vector $\mathbf{C}_h$ as shown in Figure 1. Each tube is uniquely specified by the pair of integer numbers $(L_1, L_2)$ or by its radius $R$ and chiral angle $\theta$. The latter is the angle between the chiral vector $\mathbf{C}_h$ and the nearest zigzag of carbon-carbon bonds with values in the interval $0 < \theta < \pi/6$ . The tubes are called achiral for $\theta = 0$ ("zigzag" type) and $\theta = \pi/6$ ("armchair" type), and chiral for $\theta \neq 0, \pi/6$. Every nanotube has a translational symmetry with primitive translation vector $\mathbf{T}$ connecting the point at the origin with point $(N_1, N_2)$ (see Figure 1) where $N_1 = (L_1 + 2L_2)/d$ and $N_2 = -(2L_1 + L_2)/d$. Here $d$ is the greatest common divisor of $2L_1 + L_2$ and $L_1 + 2L_2$ . The total number of atomic pairs in the unit cell is $N = N_1 L_2 - N_2 L_1$.

All the carbon atoms of a tube can be reproduced by use of two different screw operators [2, 3] (see Figure 2). The screw operator $\{\mathbf{S}|\mathbf{t}\}$ rotates the position

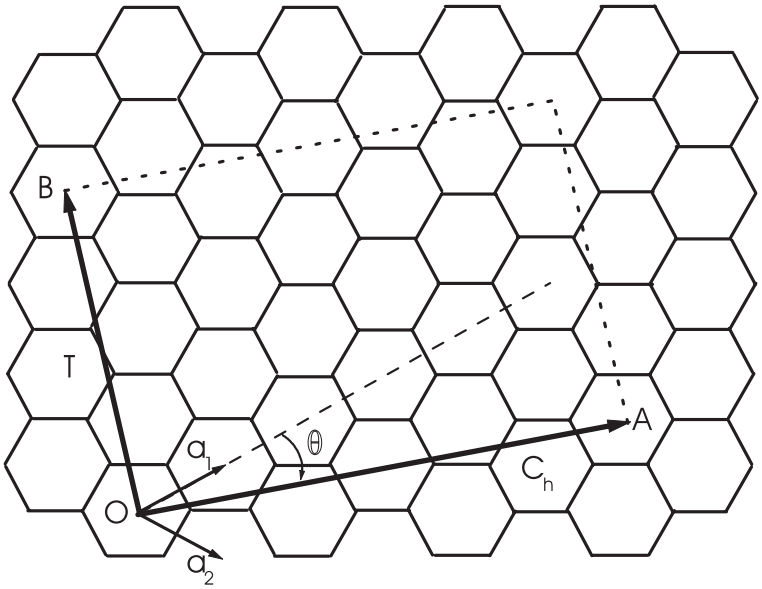


Figure 1. The honeycomb lattice of graphene. The lattice points O and A define the chiral vector Ch and the points O and B define the primitive translation vector T of the tube. The rectangle formed by the two vectors is the unit cell of the tube.

vector of an atom at an angle $\varphi$ about the tube axis and translates it at a vector $\mathbf{t}$ along the same axis. Thus, the equilibrium position vector $\mathbf{R}(\mathbf{l}\kappa)$ of the kth atom of the lth atomic pair of the tube is obtained from $\mathbf{R}(\kappa) \equiv \mathbf{R}(\mathbf{0}\kappa)$ by using of two screw operators $\{\mathbf{S}_1|\mathbf{t}_1\}$ and $\{\mathbf{S}_2|\mathbf{t}_2\}$

$$\mathbf{R}(\mathbf{l}\kappa) = \{\mathbf{S}_1|\mathbf{t}_1\}^{l_1} \{\mathbf{S}_2|\mathbf{t}_2\}^{l_2} \mathbf{R}(\kappa) = \mathbf{S}_1^{l_1}\mathbf{S}_2^{l_2}\mathbf{R}(\kappa) + l_1\mathbf{t}_1 + l_2\mathbf{t}_2 \qquad (1)$$

Here $\mathbf{l} = (l_1, l_2)$, $l_1$ and $l_2$ are integer numbers labeling the atomic pair, and $\kappa = 1, 2$ labels the atoms in the pair. It is convenient to adopt the compact notation $\mathbf{S}(\mathbf{l}) = \mathbf{S}_1^{l_1}\mathbf{S}_2^{l_2}$ and $\mathbf{t}(\mathbf{l}) = l_1t_1 + l_2t_2$, and rewrite Eq. 1 as $\mathbf{R}(\mathbf{l}\kappa) = \mathbf{S}(\mathbf{l})\mathbf{R}(\kappa) + \mathbf{t}(\mathbf{l})$. This "rolled" nanotube structure can be relaxed within tight-binding or ab-initio models. In the relaxation procedure, one usually imposes the following constraints: preservation of the translational symmetry of the tubes, keeping all atoms on one and the same cylindrical surface. As parameters of the relaxation one can choose the tube radius, the primitive translation of the tube, and the angle of rotation and the translation of the screw operation for mapping the first

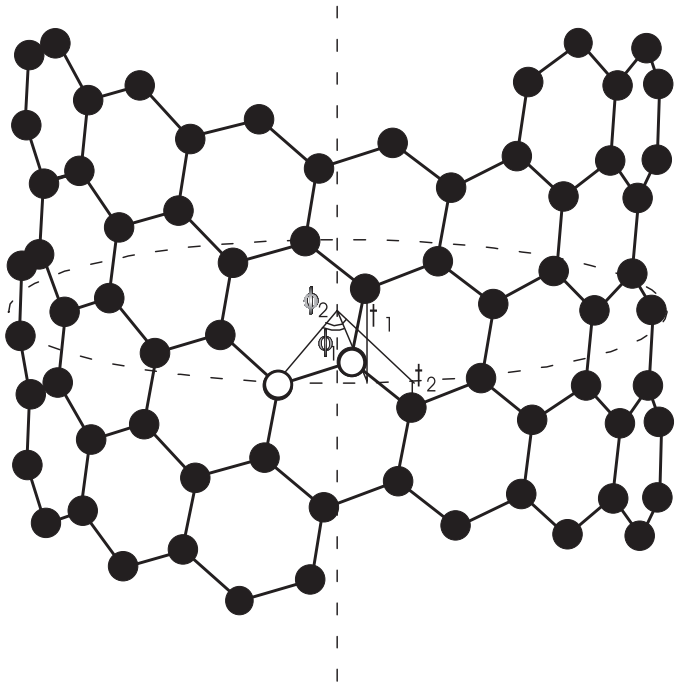


Figure 2. A front view of a nanotube. The closed dashed line is the circumference and the straight dashed line is the tube axis. The atomic pair denote by empty circles can be mapped unto the entire tube by means of two different screw operators [2].

atom of the two-atom unit cell unto the second one. The relaxed structure can be used to obtain refined values of various quantities.

## 3 Phonon Dispersion

### 3.1 The Symmetry-Adapted Lattice-Dynamical Model

The symmetry-adapted lattice dynamical model for nanotubes can be constructed as a Born model of the lattice dynamics based on a two-atom unit cell [2, 3]. In the adiabatic approximation, the atomic motion is conveniently decoupled from the electronic one. For small displacements $\mathbf{u}(\mathbf{l}\kappa)$ of the atoms from their equilibrium positions, it is customary to use the harmonic approximation and represent the atomic Lagrangian as a quadratic form of $\mathbf{u}(\mathbf{l}\kappa)$ . The equations of motion of the atoms are then readily derived in the form

$$m_\kappa \ddot{u}_\alpha(\mathbf{l}\kappa) = -\sum_{\mathbf{l}'\kappa'\beta} \Phi_{\alpha\beta}(\mathbf{l}\kappa, \mathbf{l}'\kappa') u_\beta(\mathbf{l}'\kappa') \tag{2}$$

Here $m_\kappa$ are the atomic masses and $\Phi_{\alpha\beta}(\mathbf{l}\kappa, \mathbf{l}'\kappa')$ are the force constants. The equations of motion Eq. 2 are a system of infinite number of homogeneous linear equations for the atomic displacement components. This system can be cast into a new form of finite number of equations taking advantage of the screw symmetry of the tubes. In particular, let $P(\mathbf{l})$ be the matrices of the induced representation of the screw operations symmetry group of the tube acting on $\mathbf{u}(\mathbf{l}\kappa)$ so that $P(\mathbf{l}')\mathbf{u}(\mathbf{l}\kappa) = \mathbf{u}(\mathbf{l}' + \mathbf{l}, \kappa)$. Then, it can be proven similarly to the 3d case that [4]

$$P(\mathbf{l}')\mathbf{u}(\mathbf{l}\kappa) = e^{i\mathbf{q}\cdot\mathbf{l}'} S(\mathbf{l}')\mathbf{u}(\mathbf{l}\kappa) \tag{3}$$

The atomic displacements, satisfying this condition, can be written in the form

$$u_\alpha(\mathbf{l}\kappa) = \frac{1}{\sqrt{m_\kappa}} \sum_\beta S_{\alpha\beta}(\mathbf{l}) e_\beta(\kappa|\mathbf{q}) \exp i(\mathbf{q}\cdot\mathbf{l} - \omega t) \tag{4}$$

which represents a wave with wavevector $\mathbf{q} = (q_1, q_2)$ and angular frequency $\omega(q)$. The atomic displacements remain unchanged under integer number tube translations at a distance $T$ and integer number rotations at an angle $2\pi$. These two conditions lead to the following constraints on the wavevector components

$$q_1 L_1 + q_2 L_2 = 2\pi l \tag{5}$$

$$q_1 N_1 + q_2 N_2 = q \tag{6}$$

Here $l$ and $q$ are the azimuthal quantum number and the one-dimensional wavevector of the tubes, respectively, with possible values $l = 0, 1, ..., N-1$

and $-\pi \leq q < \pi$. Using Eqs. 5 and 6, the atomic displacement Eq. 4 can be written as

$$u_\alpha(\mathbf{l}\kappa) = \frac{1}{\sqrt{m_\kappa}} \sum_\beta S_{\alpha\beta}(\mathbf{l}) e_\beta(\kappa|ql) \exp i(\alpha(\mathbf{l})l + z(\mathbf{l})q - \omega t) \qquad (7)$$

where $\alpha(\mathbf{l}) = 2\pi(l_1 N_2 - l_2 N_1)/N$ and $z(\mathbf{l}) = (L_1 l_2 - L_2 l_1)/N$ are the dimensionless coordinates of the origin of the $\mathbf{l}$th cell along the circumference and along the tube axis, respectively. Substituting Eq. 7 in Eq. 2, we get a system of six linear equations of the form

$$\omega^2(ql) e_\alpha(\kappa|ql) = \sum_{\kappa'\beta} D_{\alpha\beta}(\kappa\kappa'|ql) e_\beta(\kappa'|ql) \qquad (8)$$

where the dynamical matrix $D_{\alpha\beta}(\kappa\kappa'|ql)$ is defined as

$$D_{\alpha\beta}(\kappa\kappa'|ql) = \frac{1}{\sqrt{m_\kappa m_{\kappa'}}} \sum_{\mathbf{l}'\gamma} \Phi_{\alpha\gamma}(\mathbf{0}\kappa, \mathbf{l}'\kappa') S_{\gamma\beta}(\mathbf{l}') \exp i(\alpha(\mathbf{l}')l + z(\mathbf{l}')q) \quad (9)$$

The eigenfrequencies $\omega^2(ql)$ are solutions of the characteristic equation

$$\left\| D_{\alpha\beta}(\kappa\kappa'|ql) - \omega^2(ql)\delta_{\alpha\beta}\delta_{\kappa\kappa'} \right\| = 0. \qquad (10)$$

Substituting the solutions $\omega^2(qlj)$ ($j = 1, 2, ..., 6$) in Eq. 8, one can obtain the corresponding eigenvectors $e_\alpha(\kappa|qlj)$ ($j = 1, 2, ..., 6$). For each $q$ there are $6N$ vibrational eigenmodes (phonons) but the number of the different $\omega^2(qlj)$ can be lesser due to degeneracy. Using Eq. 9 it can be proven that $D$ is Hermitian and therefore $\omega^2(qlj)$ are real and $e_\alpha(\kappa|qlj)$ can be chosen orthonormal. Due to the explicit accounting for the screw symmetry of the tubes in the presented symmetry-adapted scheme, the computation time for each q scales as $6^3 N$. This ensures great advantage for phonon calculations of tubes with very large $N$ in comparison to the approach that does not use the screw symmetry where the computation time scales as $(6N)^3$. Practically, all observable nanotubes can be handled with the presented lattice dynamical model with respect to the numerical stability of the computations as well as to the computer memory and CPU time.

### 3.2 Phonon Dispersion, Zone-Center Phonons and Raman Intensity

The phonon dispersion of two nanotubes, calculated using force constants of valence force-field type [2, 3] is shown in Figure 3. The small number of force fields used does not allow for the precise modeling of the high-frequency branches. In particular, the "overbending" of the in-plane bond-stretching vibrations in graphene cannot be reproduced well, which results in an incorrect order of the zone-center tangential phonons in nanotubes. However, this does not affect much the low-frequency branches in nanotubes. The phonons with

wavevector $q$ inside the Brillouin zone are waves along the tube with wavelength $\lambda = 2\pi/q$. The zone-center phonons are atomic motions repeating in all unit cells along the tube. The atomic displacements for chiral tubes are not generally restricted to definite directions in space. However, the displacements for achiral tubes can be classified as radial ($R$), circumferential ($C$), and axial ($A$). The zone-center phonons of chiral tubes belong to the following symmetry species of point groups $D_N$ (Ref. [5])

$$\Gamma = 3A_1 + 3A_2 + 3B_1 + 3B_2 + 6E_1 + 6E_2 + ...6E_{N/2-1}, \qquad (11)$$

where modes $A_{1,2}$ and $B_{1,2}$ correspond to $l = 0$ and $N/2$, and modes $E_i$ correspond to $l = i$. The $E_i$ modes have $2l$ nodes around the tube circumference. The $A_{1,2}$ modes are nodeless and the $B_{1,2}$ ones have $N$ nodes. Armchair and zigzag tubes have additional symmetry elements and the modes are classified by the irreducible representations of point group $D_{2nh}$. Among the various zone-center phonons, some are infrared-active ($A_2 + 5E_1$ in chiral tubes, $3E_{1u}$ in armchair tubes, and $A_{2u} + 2E_{1u}$ in zigzag tubes), others are Raman-active ($3A_1 + 5E_1 + 6E_2$ in chiral tubes, $2A_{1g} + 2E_{1g} + 4E_{2g}$ in armchair tubes, and $2A_{1g} + 3E_{1g} + 3E_{2g}$ in zigzag tubes), and the rest are silent. The $A_{1(g)}$, $E_{1(g)}$, and $E_{2(g)}$ phonons are observed in scattering configurations $(xx + yy, zz)$,

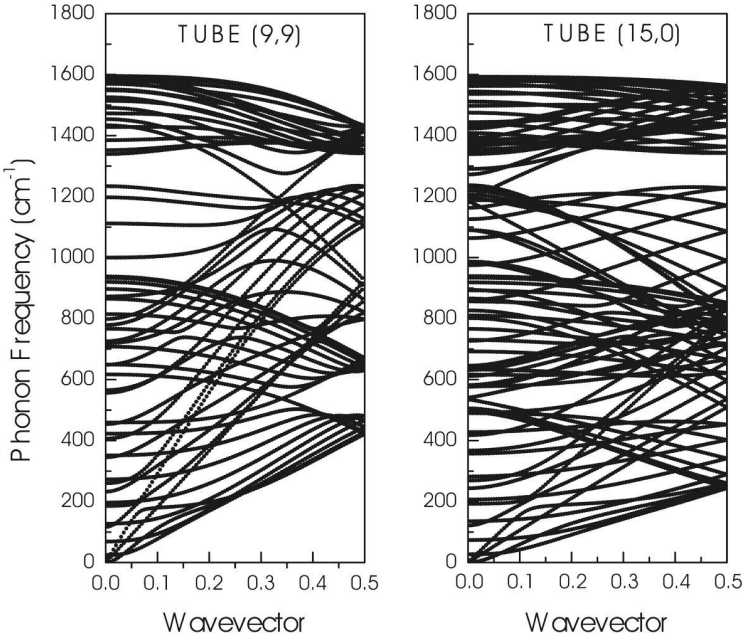


Figure 3. The phonon dispersion of nanotubes (9,9) and (15,0) calculated within a valence force field model. The number of phonon branches is 108 and 180, respectively.

$(xz, yz)$, and $(xx - yy, xy)$, respectively, for $z$ axis along the tube. (The used here Porto notation $(x_1 x_2)$ means incident light polarized along $x_1$ axis and scattered light polarized along $x_2$ axis.) Largest Raman signal is observed for parallel scattering configuration and it originates from the following $A_{1(g)}$ modes. In particular, such is a mode with a uniform radial atomic displacement (so-called radial-breathing mode or RBM) with frequency following roughly the power law $230/d$ (in cm$^{-1}$; $d$ is the tube diameter in nm); one high-frequency mode of about $1580$ cm$^{-1}$, which is purely circumferential in armchair tubes and purely axial in zigzag tubes (or two neither purely circumferential, nor purely axial modes in chiral tubes). The Raman signal due to $E_{1(g)}$ and $E_{2(g)}$ phonons is usually very weak. Apart from lines due to single-phonon processes, bands arising from more complex processes are often observed in the Raman spectra. An example of such band is the $D$ band (i.e., disorder band) due to the presence of impurities and defects in the nanotubes. The Raman lines of the high-frequency $A_{1(g)}$ modes of the different tubes are closely situated and modified by electron-phonon and electron-impurity interactions. The modeling of the latter ones also faces the problem of considering far enough neighbors in order to reproduce correctly the overbending of the phonon branches of graphene, from which these modes originate. On the other hand, the lines of the RBMs in the spectra are often well-separated and can be used for structural characterization of the nanotube samples. In bundles of nanotubes and multiwalled nanotubes, there are many breathinglike phonon modes having different Raman line intensities [6–8]. This is illustrated in Figure 4, where the Raman intensity

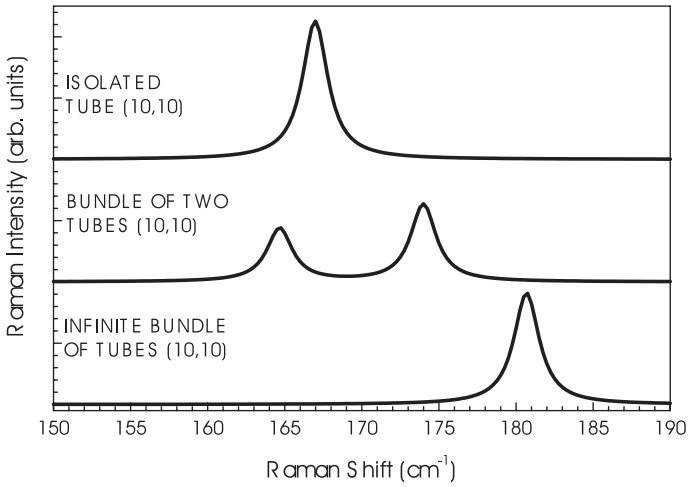


Figure 4. Non-resonant Raman intensity of an isolated nanotube, a bundle of two nanotubes, and an infinite bundles of nanotubes (10,10) calculated within a bond-polarizability model [6, 7].

of such modes of an isolated and bundled nanotubes, calculated within a bond-polarizability model, is displayed. It is clearly seen that in bundles there are more than one breathinglike mode and that the intertube interactions generally upshifts their frequencies. It has to be noted that while the bond-polarizability model describes well the non-resonant spectra of most semiconductors, the Raman spectra of nanotubes are usually measured under resonant conditions and non-resonant spectra are rarely observed because of the low signal. Any realistic calculations of the spectra should take into account the electronic band structure of the tubes (see Sec. 4).

### 3.3 Mechanical and Thermal Properties

The force constants are invariant under infinitesimal translations along and perpendicular to the tube axis that leads to the translational sum rules and to three zone-center zero-frequency modes [3] The infinitesimal rotation invariance condition imposed on the force constants gives rise to a rotational sum rule and to an additional zero-frequency mode. The former three modes are translations along and perpendicular the tube, and the latter mode is a rotation of the tube about its axis. These four modes belong to the four acoustic modes of the tube. The longitudinal and rotational acoustic branches have linear dispersion at the zone center. The corresponding acoustic wave velocities $v_L$ and $v_R$ can be associated with Young's and shear moduli of the tubes, $Y$ and $G$, as $v_L = \sqrt{Y/\rho}$ and $v_R = \sqrt{G/\rho}$ with $\rho$ being the mass density. The transverse waves have quadratic dispersion at the zone center and zero group velocity there.

The estimations of the two moduli within force-constants, tight-binding, and ab-initio models yield approximately the same value for the moduli per unit tube circumference (in-plane moduli) of about $350$ J/m$^2$ and $150$ J/m$^2$, close to the values for graphite. The Poisson ratio $\nu$ can be estimated from the expression for isotropic media $\nu = (Y/2 - G)/G$ and, for the calculated moduli, is about $0.17$. The use of different definitions for the cross-sectional area of the nanotubes can yield quite different values for the moduli. Thus, assuming a cross-section as a ring of width $0.34$ nm, one obtains $1030$ GPa and $440$ GPa slightly dependent on the tube type. For a cross-section as a full disk with radius $R$, the moduli with decrease with the increase of the radius, etc. In the case of bundles of many tubes, the cross-section should be chosen as a hexagon with area $\sqrt{3}(2R+d)^2/2$ with $d$ being the intertube separation resulting again in decreasing of $Y$ with increasing tube radius. In practice, in order to make use of the large moduli of the nanotubes, e.g., in composite materials, it is necessary to bind covalently the nanotubes in ropes and/or to the other constituents of these materials.

The bulk modulus $K$ of infinite bundles of nanotubes can be derived in a similar way as the elastic moduli of isolated tubes [9]. For small-radius tubes, $K = K_W$ is determined by the intertube forces and increases with the increase of the tube radius (see, Figure 5). For large-radius tubes, $K = K_T$ is predominantly due to

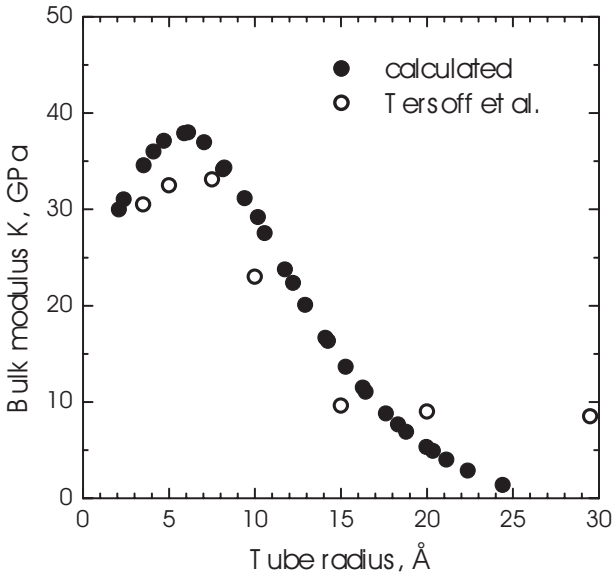


Figure 5. Bulk modulus K of infinite bundles of achiral SWNTs, calculated within a valence force-field model [9], in comparison with the one, derived in molecular dynamics simulations by Tersoff et al. [10].

the tube elasticity and decreases with the increase of the radius. For intermediate radii, $K$ can be expressed approximately as $K_W K_T/(K_W + K_T)$. The calculated $K$ from the slopes of the acoustic branches of infinite bundles of tubes agrees well with the results of the molecular-dynamics simulations [10]. The disagreement for $R > 15$ Å is due to the assumption of circular cross-section of the tubes in the former model while the intertube interactions polygonize the cross-section of large-radius tubes. The specific heat and thermal conductivity of carbon nanotubes are determined mainly by the phonons while the electronic contribution is usually negligible. The phonon specific heat of carbon nanotubes $C_v$ can be derived using the phonon frequencies calculated within the lattice-dynamical model by means of the expression [11]

$$C_v = k_B \int_0^\infty \frac{(\hbar\omega/k_B T)^2 \exp(\hbar\omega/k_B T)}{[\exp(\hbar\omega/k_B T) - 1]^2} D(\omega) d\omega, \qquad (12)$$

where $D(\omega)$ is the phonon density of states. At high temperature, $C_v$ tends to the classical limit $2kB/m \approx 2078$ mJ/gK ($m$ is the atomic mass of carbon). At low temperature, $C_v$ is determined by the dispersion of the lowest-energy acoustic branches. For one-dimensional systems, these are the transverse acoustic ones with quadratic dispersion and, therefore, $D(\omega) \propto 1/\sqrt{\omega}$ and $C_v \propto \sqrt{T}$. As it can be seen from Figure 6, this behavior can be observed below about 1 K. This

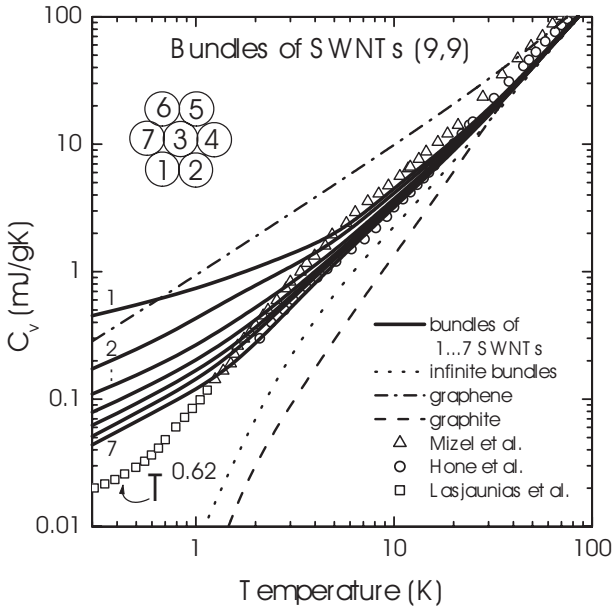


Figure 6. Specific heat of SWNTs and ropes of SWNTs, calculated within a valence force-field model [11], in comparison with that of graphene and graphite, and available experimental data by Mizel et al. [12], Hone et al. [13], and Lasjaunias et al. [14].

behavior is essentially different from that of graphene ($C_v \propto T$) and graphite and infinite bundles ($C_v \propto T^3$).

The low-temperature thermal conductivity has the same temperature behavior as the specific heat. At high temperature, scattering from the tube boundaries and *Umklapp* processes become dominant.

## 4 Electronic Band Structure

### 4.1 The Symmetry-Adapted Tight-Binding Model

The symmetry-adapted scheme can be implemented in a tight-binding model similarly to the case of the lattice dymanics [15,16]. To begin with, the electronic band structure of a periodic structure is usually obtained in the independent-electron approximation solving the one-electron Schrödinger equation

$$\left[-\frac{\hbar^2\nabla^2}{2m} + V(\mathbf{r})\right]\psi_{\mathbf{k}}(\mathbf{r}) = E_{\mathbf{k}}\psi_{\mathbf{k}}(\mathbf{r}), \tag{13}$$

where $m$ is the electron mass, $V(\mathbf{r})$ is the effective periodic potential, $\psi_{\mathbf{k}}(\mathbf{r})$ and $E_{\mathbf{k}}$ are the one-electron wavefunction and energy depending on the wavevector

$\mathbf{k}$ . This equation can be solved by representing $\psi_{\mathbf{k}}(\mathbf{r})$ as a linear combination of basis functions $\varphi_{\mathbf{k}r}(\mathbf{r})$

$$\psi_{\mathbf{k}}(\mathbf{r}) = \sum_r c_{\mathbf{k}r}\varphi_{\mathbf{k}r}(\mathbf{r}). \tag{14}$$

In the tight-binding approach, the basis function is a linear combination of the atomic orbital $\chi_r(\mathbf{R}(\mathbf{l}) - \mathbf{r})$ centered at an atom with position vector $\mathbf{R}(\mathbf{l})$ in the $\mathbf{l}$ th unit cell (the index $r$ labels the orbitals of a given atom). Substituting Eq. 14 in Eq. 13, one obtains an infinite system of homogeneous linear equations for the expansion coefficients. This system can be transformed into a finite size one taking into account the screw symmetry of the tubes. Namely, let $P(\mathbf{l})$ be the matrices of the induced representation of the screw operations symmetry group of the tube acting on $\chi_r$ so that $P(\mathbf{l}')\varphi_{\mathbf{k}r}(\mathbf{r}) = \varphi_{\mathbf{k}r}(R(\mathbf{l}') - \mathbf{r})$ . Then, it can be proven similarly to the $3d$ case that [4]

$$P(\mathbf{l}')\varphi_{\mathbf{k}r}(\mathbf{r}) = e^{i\mathbf{k}\cdot\mathbf{l}'}\sum_{r'} T_{rr'}(\mathbf{l}')\varphi_{\mathbf{k}r'}(\mathbf{r}), \tag{15}$$

where $T(\mathbf{l}')$ are rotation matrices rotating the $p$ atomic orbitals. The condition Eq. 15 can be satisfied for basis functions $\varphi$ chosen as the following linear combination of $\chi$'s [15]

$$\varphi_{\mathbf{k}r}(\mathbf{r}) = \frac{1}{\sqrt{N_c}}\sum_{\mathbf{l}r'} e^{i\mathbf{k}\cdot\mathbf{l}}T_{rr'}(\mathbf{l})\chi_{r'}(\mathbf{R}(\mathbf{l}) - \mathbf{r}) \tag{16}$$

where $\mathbf{k} = (k_1, k_2)$ is a two-dimensional wavevector and $N_c$ is the number of two-atom unit cells in the tube. The wavevector components are subject to the following constraints arising from the rotational and translational symmetry of the tube

$$k_1 L_1 + k_2 L_2 = 2\pi l \tag{17}$$

and

$$k_1 N_1 + k_2 N_2 = k. \tag{18}$$

Here $k$ is the one-dimensional wavevector of the tube ($-\pi \leq k < \pi$) and the integer number $l$ labels the electronic energy levels with a given $k$ ($l = 0, 1, ..., N-1$). The other symbols are defined in Sec. 3. Using Eqs. 17 and 18, the expansion functions can be rewritten as

$$\varphi_{klr}(\mathbf{r}) = \frac{1}{\sqrt{N_c}}\sum_{\mathbf{l}r'} e^{i(\alpha(\mathbf{l})l + z(\mathbf{l})k)}T_{rr'}(\mathbf{l})\chi_{r'}(\mathbf{R}(\mathbf{l}) - \mathbf{r}) \tag{19}$$

After substitution of Eqs. 19 and 14 in Eq. 13, the electronic problem is transformed into the matrix eigenvalue problem

$$\sum_{r'} H_{klrr'}c_{klr'} = E_{kl}\sum_{r'} S_{klrr'}c_{klr'}, \tag{20}$$

where the quantities $H_{klrr\prime}$ and $S_{klrr\prime}$ are given by

$$H_{klrr\prime} = \sum_{\mathbf{l}r''} e^{i(\alpha(\mathbf{l})l + z(\mathbf{l})k)} H_{rr''}(\mathbf{l}) T_{r''r\prime}(\mathbf{l}) \tag{21}$$

and

$$S_{klrr\prime} = \sum_{\mathbf{l}r''} e^{i(\alpha(\mathbf{l})l + z(\mathbf{l})k)} S_{rr''}(\mathbf{l}) T_{r''r\prime}(\mathbf{l}), \tag{22}$$

Here $H_{rr''}(\mathbf{l})$ and $S_{rr''}(\mathbf{l})$ are the matrix elements of the Hamiltonian and the overlap matrix elements between atomic orbitals $\chi_r(\mathbf{R}(\mathbf{0}) - \mathbf{r})$ and $\chi_{r'}(\mathbf{R}(\mathbf{l}) - \mathbf{r})$. The set of linear algebraic equations Eq. 20 has non-trivial solutions for the coefficients $c$ only for energies $E$ which satisfy the characteristic equation

$$\| H_{klrr\prime} - E_{kl} S_{klrr\prime} \| = 0. \tag{23}$$

The solutions of Eq. 23, $E_{klm}$, are the electronic energy levels; the energy bands are labeled by the composite index $lm$ ($m = 1, 2, ..., 8$ for $4$ electrons per carbon atom). The corresponding eigenvectors $c_{klmr}$ are determined from Eq. 20. Like with phonons, the symmetry-adapted approach for calculation of the electronic band structure of nanotubes has the important advantage of large reduction of the computational time. Indeed, the calculation of the band energies for a given $k$ needs time scaling as the cube of the size of the two-atom eigenvalue problem ($8^3$ for $4$ electrons per carbon atom) times the number of the two-atom unit cells $N$. On the other hand, the straightforward calculation of the same band energies will require time scaling as the cube of the size of the $2N$-atom eigenvalue problem, i.e., $(8N)^3$. For structural relaxation of a nanotube one needs the expressions for the total energy and the forces acting on the atoms. The total energy of a nanotube (per unit cell) is given by

$$E = \sum_{klm}^{occ} E_{klm} + \frac{1}{2} \sum_{ij(i \neq j)} \phi(r_{ij}), \tag{24}$$

where the first term is the band energy (the summation is over all occupied states) and the second term is the repulsive energy, consisting of repulsive pair potentials $\phi(r)$ between pairs of nearest neighbors. The band contribution to the force on the atom with a position vector $\mathbf{R}(\mathbf{0})$ is given by the Hellmann-Feynman theorem

$$\mathbf{F} = \sum_{klm}^{occ} \frac{\partial E_{klm}}{\partial \mathbf{R}(\mathbf{0})} = \sum_{klm}^{occ} \frac{\partial (H_{klrr'} - E_{klm} S_{klrr'})}{\partial \mathbf{R}(\mathbf{0})} \tag{25}$$

The repulsive contribution to the force is equal to the first derivative of the total repulsive energy with respect to the position vector $\mathbf{R}(\mathbf{0})$.

According to the simplest tight-binding model with one valence electron per carbon atom (the $\pi$-band TB model), tubes with residual of the division of $L_1 - L_2$ by $3$ equal to zero are metallic ($M$-tubes), and the remaining tubes with residual

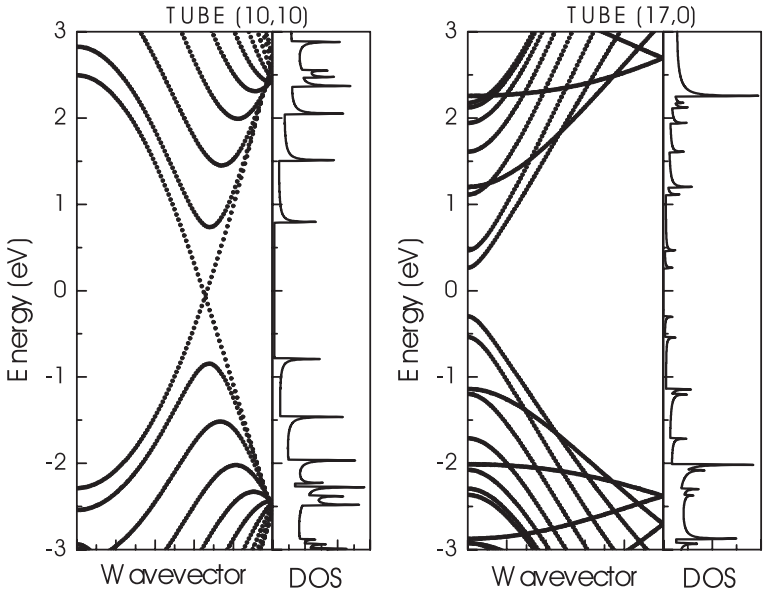


Figure 7. Band structure and electronic density of states of SWNTs (10,10) and (17,0). Notice the characteristic spikes in the electronic density of states.

1 and 2, denoted further with $Mod1$ and $Mod2$, are semiconducting ($S$-tubes). The band-structure calculations within more sophisticated models show that only armchair tubes are strictly metallic, while the remaining $M$-tubes are tiny-gap semiconductors. The results of the calculations of the band structure and the electronic density of states (DOS) for two SWNTs within a non-orthogonal tight-binding model [15, 16] (NTB model) are shown in Figure 7. Tube $(10, 10)$ is metallic with small finite density of states at the Fermi energy defined as zero. Tube $(17, 0)$ is semiconducting with a small energy gap of about $0.6$ eV. The DOS spikes have characteristic singularity at the optical transitions.

### 4.2 The Dielectric Function

The imaginary part of the dielectric function in the random-phase approximation is given by [15]

$$\varepsilon_2(\omega) = \left(\frac{2\pi e}{m\omega}\right)^2 \sum_{l'clv} \frac{2}{2\pi} \int dk \, |p_{kl'cklv,\mu}|^2 \, \delta(E_{kl'c} - E_{klv} - \hbar\omega), \qquad (26)$$

where $\hbar\omega$ is the photon energy, $e$ is the elementary charge, and $m$ is the electron mass. The sum is over all occupied ($v$) and unoccupied ($c$) states. $p_{kl'cklv,\mu}$ is the matrix element of the component of the momentum operator in the direction

$\mu$ of the light polarization

$$p_{kl'cklv,\mu} = \int d\mathbf{r}\psi^*_{kl'c}\hat{p}_\mu\psi_{klv} \tag{27}$$

Substituting Eqs. 14 and 19 in Eq. 27, one obtains the non-zero matrix elements

$$p_{kl'cklv,\mu} = f_{ll'\mu}\sum_{rr'} c^*_{kl'cr'}c_{klvr}\sum_{\mathbf{l}r''} e^{-i(\alpha(\mathbf{l})l+z(\mathbf{l})k)}p_{r'r'',\mu}(\mathbf{l})T_{rr''}(\mathbf{l}) \tag{28}$$

where

$$p_{r'r'',\mu}(\mathbf{l}) = \int d\mathbf{r}\chi_r(\mathbf{R}(\mathbf{0})-\mathbf{r})\hat{p}_\mu\chi_{r'}(\mathbf{R}(\mathbf{l})-\mathbf{r}) \tag{29}$$

For $z$-axis along the tube axis, the quantities $f_{ll'\mu}$ are given by $f_{ll'x} = f_{ll'y} = (\delta_{l',l+1}+\delta_{l',l-1})/2$ and $f_{ll'z} = \delta_{l'l}$. The latter two relations express the selection rules for allowed dipole optical transitions, namely, optical transitions are only allowed between states with the same $l$ for parallel light polarization along the tube axis and between states with $l$ and $l\prime$ differing by 1 for parallel polarization, which is perpendicular to the tube axis. In the latter case, the electronic response is much weaker than in the former due to the depolarization effect. Therefore,

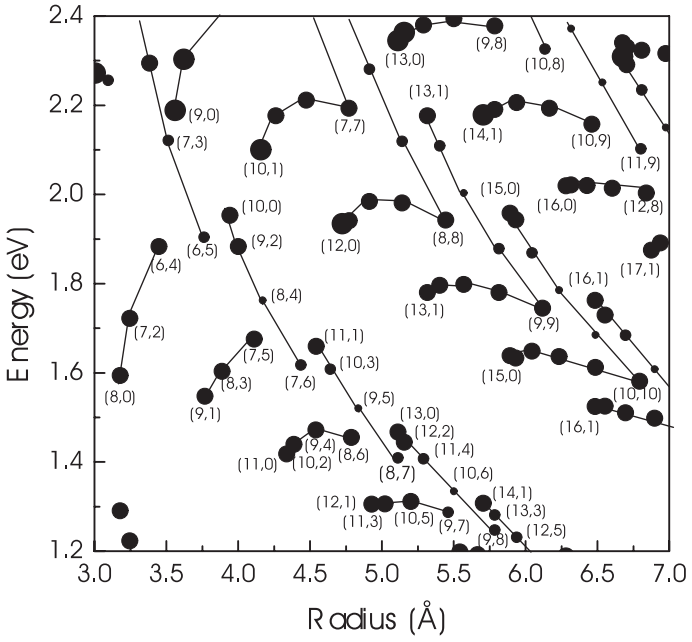


Figure 8. The resonance chart: transition energy against tube radius. Only the part, containing the points that correspond to the HiPco samples and the most frequently used laser excitation energies, is shown.

much of the efforts have been directed to the calculation of the dielectric function for parallel light polarization. The optical transition energies can be determined from the spikes of the imaginary part of the dielectric function calculated within a NTB model [15, 16]. The derived energies for parallel light polarization are shown in Figure 8 for HiPco samples and for the most frequently used laser excitation energies. The points on the plot form strips belonging to either $M$- or $S$-tubes. With increasing the energy, one crosses strips of points for transitions 11 in $S$-tubes ($Mod1$ and $Mod2$), 22 in $S$-tubes ($Mod2$ and $Mod1$), 11 and 22 in $M$-tubes (only transition 11 in armchair tubes), and so on. In each strip, the arrangement of the points show family patterns for $L_1 + 2L_2$ = integer number (connected with lines).

### 4.3 The Dynamical Matrix

The dynamical matrix of the nanotubes can be obtained from the expression of the total energy by considering the change of the energy arising from a given static lattice deformation (a phonon). The derivation is too involved to be shown here and the same holds true for the final expression of the dynamical matrix. Here, it suffies to provide results of the calculations for particular nanotubes. We note that this method is not applicable to armchair tubes because the dynamical matrix has a logarithmic singularity at the band crossing at the Fermi energy. The tiny-gap $M$-tubes require large number of $k$-points to ensure convergence of the sum over the Brillouin zone in the expression of the dynamical

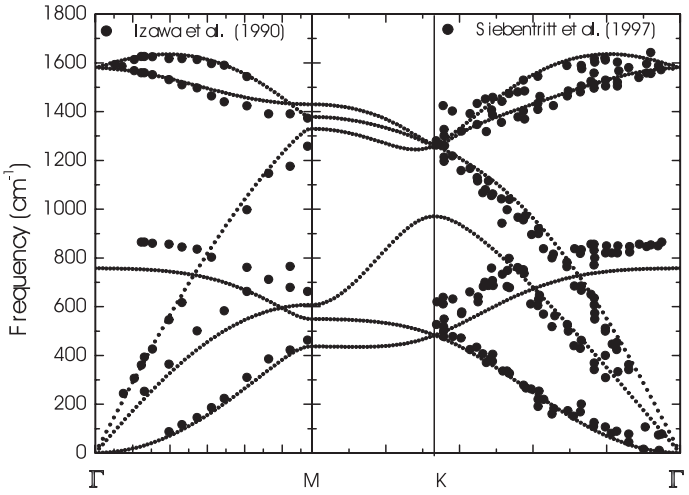


Figure 9. Phonon dispersion of graphite calculated within a NTB model and scaled by a factor of 0.9 in comparison with available experimental data by Izawa et al. [18] and Siebentritt et al. [19].

matrix. This problem does not normally appear for $S$-tubes where a moderate number of $k$-points is sufficient. The calculated phonon dispersion of graphene within the NTB model overestimates the measured one by about $10\%$. The calculated frequencies, multiplied by $0.9$, are shown in Figure 9. It is clear that the overbending of the highest-frequency branches is well reproduced while the out-of-plane optical branch is now underestimated. Since we are rather interested in the former one, the underestimation for the latter one will not be important.

As it was mentioned above, the RBM is of primary importance for the structural characterization of the samples. In Figure 10, the calculated RBM frequency of all tubes in the radius range from 2 Å to 12 Å is shown in comparison with available ab-initio results for strictly radial atomic displacements. The points follow a power law $1141/R$ (in cm$^{-1}$, $R$ in Å). In the presence of impurities and structural disorder, there is an additional light-scattering mechanism, so-called double resonance mechanism. It is responsible for the specific Raman line broadening and the position shift with the laser excitation energy especially observed for the $D$ (disorder), $G$, and $G'$ bands. The review of this mechanism lies outside the scope of this paper.

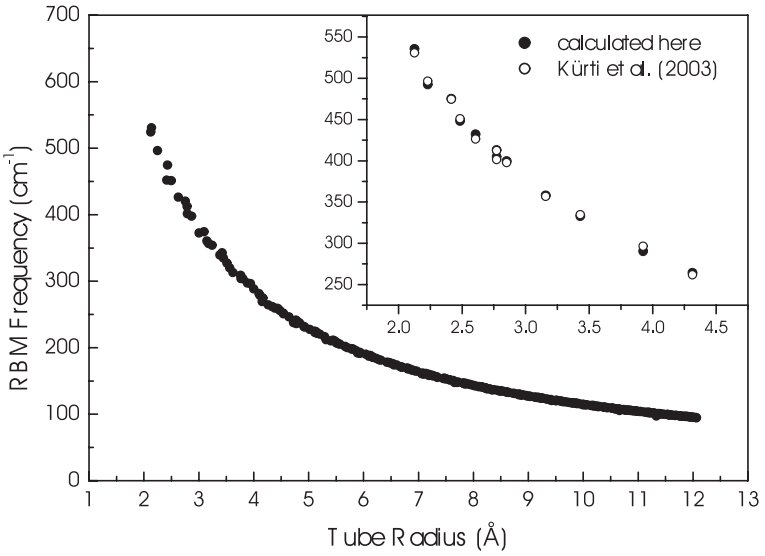


Figure 10. Calculated RBM frequencies within a NTB model vs tube radius. The comparison with ab-initio results by Kürti et al. [20] reveals disagreement less than 5 cm-1 (see inset).

### 4.4 The Resonant Raman Intensity

The Raman-scattering process can be described quantum-mechanically considering the system of the electrons and phonons of the tube and the photons of the electromagnetic radiation and their interactions [21]. The most resonant Stokes process includes a) absorption of a photon (energy $E_L$, polarization vector $\epsilon_L$) with excitation of the electronic subsystem from the ground state with creation of an electron-hole pair, b) scattering of the electron (hole) by a phonon (frequency $\omega_o$, polarization vector $\mathbf{e}$), and c) annihilation of the electron-hole pair with emission of a photon (energy $E_S = E_L - \hbar\omega_o$, polarization vector $\epsilon_S$) and return of the electronic subsystem to the ground state. The Raman intensity for the Stokes process per unit tube length (the so-called resonance Raman profile or RRP) is given by [22] (up to a slightly tube-dependent factor)

$$I(E_L, \omega_o) \propto \left| \frac{1}{L} \sum \frac{p_{cv}^S D_{cv} p_{cv}^{L*}}{(E_L - E_{cv} - i\gamma_{cv})(E_S - E_{cv} - i\gamma_{cv})} \right|^2, \qquad (30)$$

where $L$ is the length of the tube containing $N_c$ unit cells, $E_{cv} = E_c - E_v$, $E_c$ and $E_v$ are energy levels in the valence band $v = klm$ and the conduction band $c = klm\prime$, and $\gamma_{cv}$ is the excited state width. $p_{cv}^{L,S}$ is the matrix element of the component of the momentum in the direction of the polarization vector $\epsilon^{L,S}$ . The electron-phonon coupling matrix element $D_{cv}$ is determined by the scalar product of the derivative of $E_{cv}$ with respect to the atomic displacement vector $\mathbf{u}$ and the phonon eigenvector $\mathbf{e}$

$$D_{cv} \propto \sqrt{\frac{\hbar}{2m\omega_o}} \sum_{i\gamma} e_{i\gamma} \frac{\partial E_{cv}}{\partial u_{i\gamma}}. \qquad (31)$$

Here $m$ is the mass of the carbon atom and $u_{i\gamma}$ is the $\gamma$ -component of the displacement of the $i$th atom in the two-atom unit cell. The derivatives with respect to the atomic displacements for the considered phonon can be calculated using the Hellmann-Feynman theorem. The estimation of the Raman intensity can be simplified for well-separated features of the RRPs within two approximation schemes. In the first scheme, one considers the matrix elements in Eq. 30 as $k$-independent and pulls them out of the summation. The remaining summation can be performed analytically. The obtained RRPs reproduce within $5\%$ the results of the full calculations using Eq. 30. In the second scheme, one considers the matrix elements as k-independent and tube-independent (i.e., constants) and evaluates the remaining sum analytically. Based on extensive calculations, it was shown that the tube-independent scheme often leads to erroneous predictions of the Raman intensity and should therefore be avoided [22, 23]. This is illustrated in Figure 11 in the case of three tubes with close radii. Once the RRPs are evaluated for all nanotube types present in the measured samples, the Raman spectra for different laser excitation energies can be simulated using the

following expression [22]

$$I_{tot}(E_L,\omega) = \sum g I(E_L,\omega_o)\frac{1}{(\omega-\omega_o)^2+\gamma_o^2} \tag{32}$$

where $g$ is the tube distribution function for the given sample, $\gamma_o$ is phonon linewidth (HWHM), and the summation is carried out over all tube types. The usually adopted Gaussian distribution does not describe sufficiently well the tube types present in the samples. In this case, Eq. 32 can be fit to the measured spectra at several laser excitation energies to obtain the distribution function. The maximum Raman intensities can be plotted for better visualization as circles with size proportional to the logarithm of the intensity on the transition energy - tube radius plot. As it is seen in Figure 8, in each strip, the lower part of the points has larger intensity than the upper one. Thus, the points belonging to transitions 11 in $S$-tubes ($Mod1$), 22 in $S$-tubes ($Mod2$), 11 in $M$-tubes ($Mod0$) including transitions 11 in armchair tubes have larger intensity than their counterparts in the strips. This general behavior is corroborated by recent Raman data [24, 25].

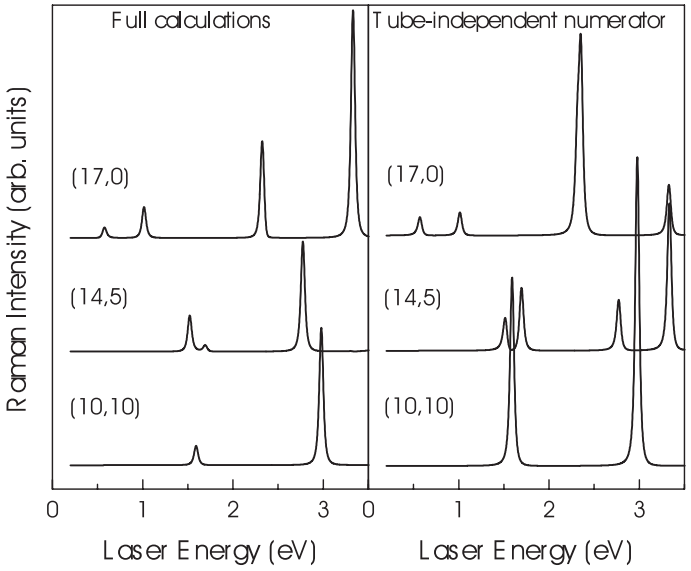


Figure 11. RBM resonance Raman profiles of three different tubes with radius of about 6.7 Å: (17,0), (14,5), and (10,10). The results of the full calculations (Eq. ) are compared to those of the frequently used tube-independent numerator approximation.

## 5 Conclusions

It is shown that the atomistic approach to the study of the vibrational, mechanical, thermal, electronic, optical, dielectric, etc., properties of ideal nanotubes can be successful when exploiting the screw symmetry of the nanotubes. The results of the calculations of some of these properties using the symmetry-adapted scheme are discussed in comparison with available theoretical and experimental data.

## Acknowledgments

V. N. P. was supported partly by a Marie-Curie Intra-European Fellowship MEIF-CT-2003-501080 and partly by a NATO CLG 980422. This work was partly funded by the Belgian Interuniversity Research Project on quantum size effects in nanostructured materials (PAI-IUAP P5/1). V. N. P. and Ph. L. were partly supported by the NATO CLG 980422.

## References

[1] M.S. Dresselhaus, G. Dresselhaus, and Ph. Avouris, eds. (2001) *Carbon nanotubes: Synthesis, Structure, Properties, and Applications* (Springer-Verlag, Berlin).
[2] V.N. Popov, V.E. Van Doren, and M. Balkanski (1999) *Phys. Rev. B* **59** 8355.
[3] V.N. Popov, V.E. Van Doren, and M. Balkanski (2000) *Phys. Rev. B* **61** 3078.
[4] J.W. Mintmire and C.T. White (1995) *Carbon* **33** 893.
[5] O.E. Alon (2001) *Phys. Rev. B* **63** 201403.
[6] V.N. Popov and L. Henrard (2001) *Phys. Rev. B* **63** 233407.
[7] L. Henrard, V.N. Popov and A. Rubio (2001) *Phys. Rev. B* **64** 205403.
[8] V.N. Popov and L. Henrard (2002) *Phys. Rev. B* **65** 235415.
[9] V.N. Popov, V.E. Van Doren, and M. Balkanski (2000) *Solid State Commun.* **114** 395.
[10] J. Tersoff and R.S. Ruoff (1994) *Phys. Rev. Lett.* **73** 676.
[11] V.N. Popov (2002) *Phys. Rev. B* **66** 153408.
[12] A. Mizel, L.X. Benedict, M.L. Cohen, S.G. Louie, A. Zettl, N.K. Budraa, and W.P. Beyermann (1999) *Phys. Rev. B* **60** 3264.
[13] J. Hone, B. Batlogg, Z. Benes, A.T. Johnson, and J.E. Fischer (2000) *Science* **289** 1730.
[14] J.C. Lasjaunias, K. Biljakovic, Z. Benes, J.E. Fischer, and P. Monceau (2002) *Phys. Rev. B* **65** 113409.
[15] V.N. Popov (2004) *New J. Phys.* **6** 17.
[16] V.N. Popov and L. Henrard (2004) *Phys. Rev. B* **70** 115407.
[17] J. Maultzsch, S. Reich, and C. Thomsen (2002) *Phys. Rev. B* **65** 233402.
[18] T. Izawa, R. Souda, S. Otani, Y. Ishizawa, and C. Oshima (1990) *Phys. Rev. B* **42** 11469.

[19] S. Siebentritt, R. Pues, K.-H. Rieder, A.M. Shikin (1997) *Phys. Rev. B* **55** 7927.
[20] J. Kürti, V. Zólyomi, M. Kertesz, and G. Sun (2003) *New J. Phys.* **5** 125.
[21] R. Loudon (1963) *Proc. Roy. Soc. London* **275** 218.
[22] V.N. Popov, L. Henrard, and Ph. Lambin (2004) *Nano Letters* **4** 1795.
[23] V.N. Popov, L. Henrard, and Ph. Lambin (2005) *Phys. Rev. B* to appear.
[24] C. Fantini, A. Jorio, M. Souza, M.S. Strano, M.S. Dresselhaus, and M.A. Pimenta (2004) *Phys. Rev. Lett.* **93** 147406.
[25] H. Telg, J. Maultzsch, S. Reich, F. Hennrich, and C. Thomsen (2004) *Phys. Rev. Lett.* **93** 177401.